J. Fluid Mech. (2010), *vol.* 651, *pp.* 55–80.
doi:10.1017/S0022112009993776

Experimental study of the behaviour of mini-charge underwater explosion bubbles near different boundaries

C. F. HUNG[1] AND J. J. HWANGFU[2]†

[1]Department of Engineering Science and Ocean Engineering, National Taiwan University, 1, Section 4, Roosevelt Road, Taipei, 106, Taiwan

[2]Chung Shan Institute of Science and Technology Chemical System Division, P.O. Box 90008-17 Longtan, Taoyuan County, 325, Taiwan

(Received 16 January 2009; revised 28 November 2009; accepted 4 December 2009; first published online 7 April 2010)

This work experimentally studies the behaviour of underwater explosion bubbles near different boundaries. The results are compared with theoretical and experimental data on cavitation bubbles. Although explosion and cavitation bubbles behave similarly on a macroscopic level, there are still some differences, most of which are from the explosive nature of the explosion bubble. The relationship between bubble migration and the Kelvin impulse, surface inertia m^* and surface stiffness k^* is investigated. We found that none of them comprehensively predicts the migration of both cavitation and explosion bubbles when boundary elasticity is considered. This elasticity should be considered as a relative value with respect to bubble size. On the other hand, the phase between local vibration of boundaries and the pulsation of bubbles could be a useful predictive index of bubble migration. When using research results developed for cavitation bubbles in relation to explosion bubbles, the material presented here may be useful for pointing out their similarities and differences.

1. Introduction

Bubbles appear in various physical and engineering problems and have been studied by scientists for many years. The first theoretical approach for a spherical bubble was presented in basic work by Rayleigh (1917). Both underwater explosions (UNDEX) and cavitation bubbles possess destructive features and due to military and industrial needs they were studied very early. The damageability of these two bubbles is related to their collapse mechanism and their macroscopic behaviour is similar; as a result, they are usually discussed together.

Bubbles can be characterized by their period, radius or shape variation, migration, jet and bubble pulse. The period and radius variation of a bubble in a free field can be computed by using the Rayleigh–Plesset equation. Although this equation involves many assumptions, it can adequately predict bubble dynamics for a bubble life of one expansion/contraction cycle for both an UNDEX and a cavitation bubble.

During World War II, military needs motivated large-scale research into UNDEX, most of which focused on basic properties of explosives, such as the peak pressure of explosion shock waves or the primary shock, the bubble pulses, the bubble periods

† Email address for correspondence: sandy.hwangfu@msa.hinet.net

and the bubble behaviour near boundaries. After the war, Cole (1948) collected the research of the period in the classic *Underwater Explosions*. In the meantime, cavitation problems emerged, where small bubbles induced by low pressure formed pits on the surface of hydraulic machines, reduced their efficiency, further motivating research. In 1961, Naude & Ellis first observed the jet phenomenon in a bubble near a rigid wall in a flowing channel. They hypothesized that it was this jet that caused cavitation damage.

Because jets have the same direction as bubble migration, the research on UNDEX bubbles shows that they migrate towards rigid boundaries and away from free surfaces. It is possible that a flexible material coated on the surface of machine can produce a neutral collapsing bubble, which will not migrate towards boundaries, and thus can prevent cavitation damage. This idea encouraged research into the influence of boundaries on bubbles.

When a gravitational field and/or a boundary are added into a free field, the bubble will become aspheric and the assumptions of the Rayleigh–Plesset equation do not hold. Plesset & Chapman (1971) used a boundary element method (BEM) to cope with this problem. They simulated the jet formation in a bubble near a rigid wall. After this, BEM was widely used in both UNDEX and cavitation bubble simulation. Difficulties in the simulation of bubbles, such as toroidal shapes, jet penetration and jet splashing, were solved by the contributions of Gibson & Blake (1982), Blake, Taib & Doherty (1986, 1987), Best (1993), Tong *et al.* (1999) and Lee, Klaseboer & Khoo (2007). In the case of UNDEX, Wilkerson (1993) and Hooton *et al.* (1993) made significant contributions.

Bubble migration direction can be predicted by the Kelvin impulse. Blake & Cerone (1982) first used potential flow and the image method to develop a theory to compute the Kelvin impulse of a bubble near a rigid wall, free surface and inertia boundary. The additional work of Blake *et al.* (1986, 1987), Blake & Gibson (1987) and Best & Blake (1994) increased the sophistication of the computation.

The bubble that Naude & Ellis (1961) observed was moving along stream. This is not an effective way to carry out an experiment, especially when boundaries are being studied. Sparks and lasers were introduced to generate one 'stationary' bubble near a boundary. The behaviour of one bubble near a rigid and free surface was investigated by Lauterborn & Bolle (1975) and Tomita & Shima (1986). The more complex behaviour of bubbles near non-rigid boundaries was investigated by Gibson & Blake (1982), Shima *et al.* (1989), Brujan *et al.* (2001*a*, 2001*b*), Tomita & Kodama (2003) and Lindau & Lauterborn (2003). Gibson & Blake (1982) introduced boundary inertia m^* and boundary stiffness k^*, the latter of which was the first use of a quantitative elastic factor that described a boundary.

The experimental works on UNDEX bubbles are mainly concerned with rigid wall boundaries; see for example Goertner, Hendrickson & Leamon (1969) or Menon (1996). Studies that involved elastic boundaries mostly focused on the dynamic responses of a flat plate subjected to a primary shock; see for example Rentz (1984), Ramajeyathilagam Vendhan & Rao (2000), Rajendran & Narasimhan (2001), Hung & Hsu (2003), Ramajeyathilagam & Vendhan (2004) and Hung, Hsu & Hwangfu (2005). Klaseboer *et al.* (2005) observed the behaviour of UNDEX bubbles near rigid and resilient boundaries. This was the first UNDEX treatment of an elastic boundary, but only one boundary and one stand-off was employed.

By the nature of the image method, a flexible boundary cannot be simulated. A finite element method (FEM) with an arbitrary Lagrange–Eulerian (ALE) algorithm can handle this problem, but is computationally expensive when simulating the fluid

domain. Menon (1996) and Chisum & Shin (1997) adopted the ALE method for UNDEX bubble simulation. A more economical way is coupled BEM/FEM, which was adopted by Hammond & Grzebieta (2000) and Klaseboer *et al.* (2005). Hung *et al.* (2003, 2005) used BEM/FEM to analyse the response of a plate to different input shock waves and bubble pulses for various stand-offs. The feasibility of a short stand-off computation using BEM/FEM in comparison with experimental results was examined. In cavitation studies, Duncan, Milligan & Zhang (1996) simulated Shima *et al.*'s (1989) experiments with excellent results.

Because many papers have discussed UNDEX and cavitation bubbles simultaneously, it is not surprising to find that researchers applied materials developed for cavitation bubbles to UNDEX bubble research. However, there are some important differences between the two. The source of the UNDEX bubble is an explosion, while the sources of experimental cavitation bubbles are focused lasers or electric sparks. Explosion is a more violent method than lasers or sparks; the peak value of the primary shock is at least six times greater than the bubble pulse, while for the laser bubble it is approximately the same (Vogel & Lauterborn 1988; Tong *et al.* 1999). This implies that the UNDEX bubble may have higher energy content than a spark/laser bubble. Primary shock can induce pronounced boundary responses; the interactions between these responses and bubble motions are inherent characteristics of an UNDEX bubble near a boundary and will not be observed in a laser or spark bubble. The contents of a spark/laser bubble are all derived from water. When bubbles contract, all of their reaction products may dissolve in the surrounding water under the high pressure and temperature conditions inside the bubble (Didenko & Suslick 2005). The contents of an UNDEX bubble depend on the explosive, and most of them will not dissolve in the water when the bubble contracts.

In this work, the authors explore the differences and similarities of UNDEX and cavitation bubbles through an experiment. The experiment was conducted in a steel tank; a detonator was used as the bubble source; different square plates were used as boundaries; strain gauges were installed on the plate to measure its responses; high-speed photography was used to capture images of the bubble; and a pressure gauge was used to measure the primary shock and bubble pulse. The details of the UNDEX bubble behaviour were analysed and compared with a cavitation bubble. The results show that the differences in the bubble period and radius variation between the two bubbles are influenced by heat transfer. Similarities include the trend of bubble period and collapse position when near a boundary, and are strongly influenced by stand-off. The Kelvin impulse, boundary inertia m^* and the boundary stiffness k^* were computed to investigate their relation to bubble migration. We cannot find a good correlation between these parameters and the prediction of the migration for cavitation and explosion bubbles when elasticity of the boundary is considered. On the other hand, from the strain measurements it was found that the phase between local vibration of the boundary and bubble pulsation could be a useful predictive index for bubble migration.

2. Experimental procedure

Figure 1 shows a sketch of the experimental arrangement used in this study. The water tank had dimensions of $4 \times 4 \times 4$ m and was made from 10 mm steel plates and filled up with tap water. A 0.8×0.9 m acrylic window was installed on each face of the tank wall.

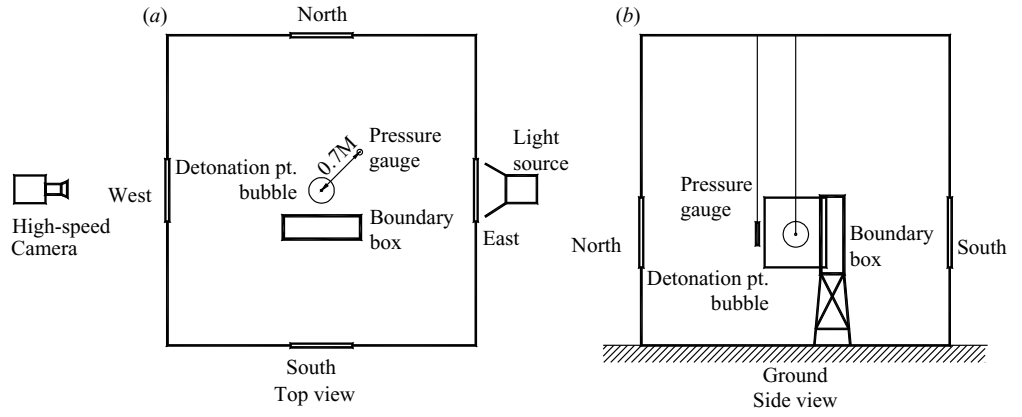

FIGURE 1. Experimental arrangement.

2.1. *Bubble*

Bubbles were generated by a detonator. This detonator is a standard ignition source for laboratory use and is manufactured with great precision. The type and weight of the explosive and the dimension of the detonator were known. Because the chemical reaction speed of the explosive was in the order of microseconds ($1\ \mu s = 10^{-6}$ s), much faster than the bubble motion, it can be assumed that the solid explosive became gas immediately after ignition. In other words, the initial volume of the bubble could be estimated. This is beneficial when solving the Rayleigh–Plesset equation. The fire unit is a reliable high-energy system, which promises a complete reaction. The error of the weight of the explosive used in the detonator was below 0.35 %. These factors permitted the creation of a stable, high-quality UNDEX bubble in the experiments.

2.2. *Test boundary*

Three square plates, each with 1 m edges, were used as the test boundary plates. They were composed of 5 mm and 10 mm thick aluminium (Al) and 35 mm thick steel (St). Each plate was clipped on a $1 \times 1 \times 0.235$ m heavy steel box. The box was empty and dry inside (air-backed) and was placed on a rack in the tank. Because the stiffness and the mass of the plates were much less than those of the box, the plates were regarded as fixed in six degrees of freedom on four sides.

2.3. *Test conditions*

The detonator was placed on the normal line through the centre of the boundary plate. The position of the boundary box was adjusted so the explosion bubble could be seen in the window. The detonation depth D was 2.55 m. The distance between the detonator and the boundary is termed the stand-off and is denoted by L. The maximum bubble radius, R_{MAX}, was used as the characteristic length. L was varied from 0.5 to 4 times R_{MAX}.

Three extra experiments are considered for comparison. The first two are free field (FF) and free surface (FS) experiments. The third one used a free hung $1\ \text{m} \times 1\ \text{m} \times 10$ mm thick Al plate as a boundary. Both faces of the plate were immersed in water (2 face immersed, 2FI). This arrangement was similar to Klaseboer *et al.*'s (2005) vertical steel plate experiment. The 2FI and some of the FF experiments were performed earlier and at that time the depth of the test tank was 3 m and D was 1.5 m. For the FS experiment, D was 0.28 m. Table 1 lists the parameters of experiment at each boundary condition.

Boundary condition	Boundary material	Boundary plate thickness (mm)	Stand-off (mm)	Detonation depth D (m)
Free field	none	–	–	1.50
				2.55
Free surface	Air	–	283	0.28
Two-face immersed plate	Aluminium plate	10	123, 134	1.50
Air-backed four-side clipped plate	Aluminium plate	10	82, 90, 135, 159, 343, 349, 700	2.55
		5	103, 149, 264, 270, 310	2.55
	Steel plate	35	159, 249, 281, 293, 320	2.55

TABLE 1. Test parameters at each boundary condition.

Machine	Test condition	Size of image area (mm)	Resolution (w × h) (pixel)	Error range (500/w*2) (mm)	Accuracy (Error range/R_{MAX}) (%)
1	FF	500 × 500	478 × 478	2.09	1.27
1	2FI		478 × 478	2.09	1.27
1	10 mm Al		330 × 330	3.03	1.84
2	5 mm Al		192 × 192	5.21	3.16
2	35 mm St		213 × 213	4.69	2.84
2	FS		194 × 194	5.15	3.12

TABLE 2. Accuracy of image under different test conditions.

2.4. *High-speed photography*

A high-speed photography machine was used to take images of bubble motions. The machine was placed at least 10 m away from the tank's west window to reduce image distortion. A strong light was installed at the east window. Because the bubble surface occludes the view of its interior, a shadow graphic method was used. A steel wire grid of size 0.8 m × 0.8 m with 5 cm square mesh was first placed at the detonation point and a few frames were taken before the test. After that, the machine position and the setting were not changed. From the image of the grid, the dimensions of the image were calibrated.

The accuracy of high-speed photography depends on many factors. Because the relative position of the machine to the tank and the zooming set-ups were different every day and two different machines were used throughout the experiments, the area shown in the images was different. For all conditions, a unified 500 mm × 500 mm area was trimmed before the image analysis; table 2 shows the resolutions and parameters relating to the accuracy of the analysis. The frame rate varied from 1000 to 5000 f.p.s., depending on the capacity of the machine and test requirements.

2.5. *Instrumentation*

Two micro-measurement rosette strain gauges were installed on the dry side of the boundary plate in the centre. The strain variations measured from each arm were almost identical, which suggests that the deformation around the plate centre was uniform in all directions (Hwangfu 2004). One PCB model 138A underwater blast pressure gauge was dipped into water to the same depth as the detonator to measure

pressure variation. The distance from the pressure gauge to the detonator was 0.7 m in the boundary test and 1.4 m in the FF test.

The strain and pressure gauges have their own signal conditioners and transient recorders. Signals were first sent to the signal conditioner and then sent to the transient recorder. The resolution the strain gauge recorder was 12 bit and that of the pressure recorder was 8 bit. The sampling rate for both was approximately 6.7 MHz.

2.6. *Data processing and accuracy*

High-speed photographic images were first digitized, and then the contour of the bubble was traced. From the contour lines, the coordinate of the highest, lowest, leftmost and rightmost points of the bubble was measured along with the tip of the bubble protrusion. From these coordinates the radius variation, bubble expansion/contraction and jet tip speed were computed. Under FF and FS conditions, the bubble was axially symmetrical; the distance between the upper and lower points, or the leftmost and rightmost points, was the diameter. Under other test conditions, the bubble possessed plane symmetry and the distance between those points could not be treated as the diameter; therefore the term 'margin difference' was used instead. The error range of the diameter or margin difference was approximately two pixels of image. Table 2 also shows the error ranges of each test condition. The average R_{MAX} is denoted as R_{MAX0}. Under the FF condition at $D = 1.5$ m, R_{MAX0} is 171.24.2 mm, and at 2.55 m R_{MAX0} is 163.84.2 mm, which is equal to 1.32 g of TNT exploded for the same D. The non-dimensional stand-off γ used in this paper is scaled to R_{MAX0}:

$$\gamma = \frac{L}{R_{MAX0}}. \tag{1}$$

For speed measurements, shutter speed is usually considered because the image is the 'shadow' that the bubble has moved through during the period when the shutter opened. When the bubble expands the shadow becomes bigger monotonically, the contour lines are the final position of the bubble margin when the shutter closed, so the errors of speed all come from the measurement of diameter or margin difference. For the same reason, this accuracy can be applied to contraction speed, except at the moment of collapse.

The estimation of accuracy of the measurement of the transient recorder is very difficult. A simple estimation of error is the physical quantities presented by one count of the recorder's A/D convertor, and to assume that the error in the time sequence is negligible. In this way, for a 12 bit resolution strain gauge recorder the error is approximately ± 2 micro-strain ($\mu\varepsilon$, $1\,\mu\varepsilon = 10^{-6}$ strain). The range of pressure measurement is from -1.0×10^6 to 3.0×10^6 Pa (-145 to 435 psi), so the error of the pressure data is approximately $\pm 15\,600$ Pa (± 2.27 psi) at 8 bit resolution. Figure 2 shows the image of bubble motion under the FF condition. Figure 3(a) shows the time history of radius and pressure variations at this condition. The period between the wavefront of the primary shock and the peak of the first bubble pulse was measured as the bubble period, t_B. The average t_B under the FF condition at $D = 1.5$ m is 28.93 ms, and at 2.55 m is 27.13 ms; this is equivalent to 1.12 g of TNT.

The pressure history in figure 3(a) is quite noisy. The fluctuations are especially striking in the beginning of the bubble expansion and fade away when the bubble contracts. This noise is the reflections of the primary shock from the walls and free surface. Figure 3(b) is a close-up of figure 3(a) from the time 0.0–4.0 ms; we can see a clear shock wave with less noise before 1.2 ms, after which the reflected waves come and the pressure pattern becomes noisy.

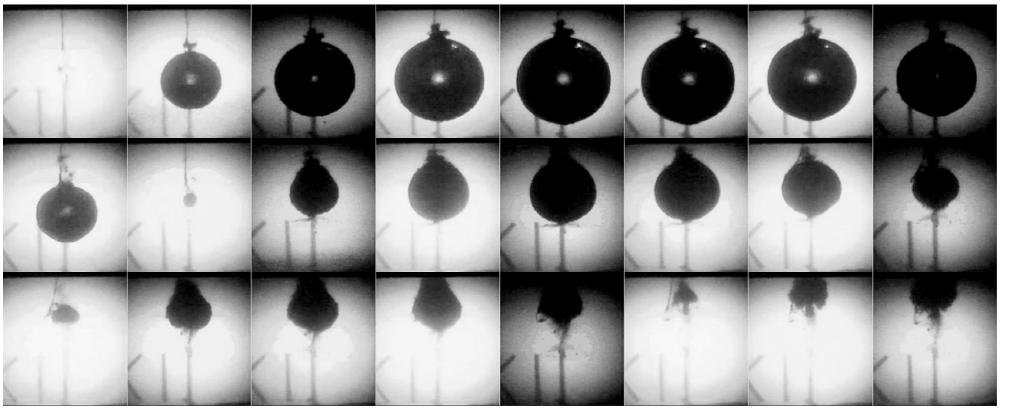

FIGURE 2. High-speed photograph of bubble motion under FF conditions ($D = 1.5$ m, frame interval = 3 ms, image width = 500 mm).

The distance from the detonation point to the pressure gauge is 1.4 m, and the sound speed in water is about 1500 m s^{-1}; the time when the shock wave begins is about 0.93 ms before $t = 0.0$ ms. The distances between tank walls and the detonation point are 2 m, the distances from the bottom and free surface to the detonation point are 1.5 m. The earliest group of reflection waves around $t = 1.2$ ms is the first reflections from the north, east wall and bottom. The next group of peaks around $t = 1.9$ ms is the waves that first impinge on the bottom and then rebound from the north and east walls. The peaks around $t = 2.7$ ms are the first reflections from the west and south walls. The negative pressure between $t = 1.2$–2.7 ms is the rarefaction wave reflected from the free surface. After $t = 2.7$ ms, the multi-reflected waves are mixed together, and no further identification can be made.

The tank wall is made of steel so the amplitude of the reflection is high. All these reflection waves decay very fast; when the bubble pulse comes, the pattern has become clear. The interference between these and the dynamics of the bubble can be estimated from the work done in the bubble expansion:

$$W = \int_{R_0}^{R_{\mathrm{MAX}}} 4\pi R^2 p \mathrm{d}R, \tag{2}$$

where p is the ambient pressure in water. In the ideal case $p = p_{atm} + p_H - p_v$, where p_{atm} is the atmospheric pressure, p_H is the hydraulic pressure and p_v is the vapour pressure inside bubble which can be determined from the water temperature using steam tables (Keenan *et al.* 1969). In this experiment, contributions due to the reflected wave p_r should be added to (2), which becomes

$$W = \int_{R_0}^{R_{\mathrm{MAX}}} 4\pi R^2 (p_{atm} + p_H - p_v + p_r) \mathrm{d}R, \tag{3}$$

where p_r is not known; however, the time history of pressure measured 1.4 m away from the bubble is known. Assuming that the bubble experiences similar pressure, (3) can be numerically computed as

$$W \cong \sum_{t_i = t_{ARR}}^{t_i = t_{MAX}} 4\pi R^2(t_i) \left[p_{atm} + p_H - p_v + p_r(t_i)\right] \left[R(t_i) - R(t_{i-1})\right] = W_0 + W_r, \tag{4}$$

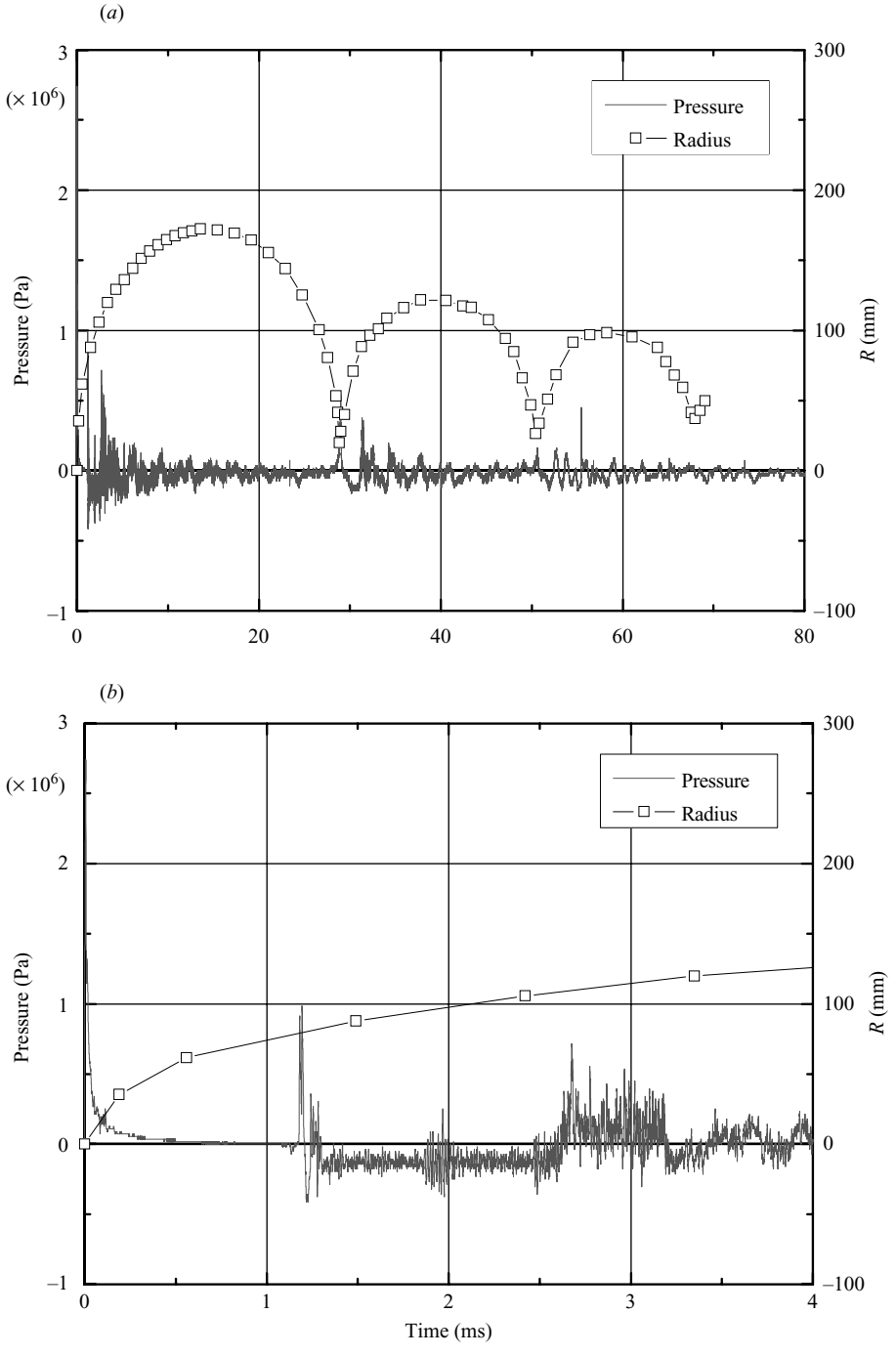

FIGURE 3. (*a*) Radius and pressure variations of an FF bubble. The maximum radii and periods for the first cycle are 171 mm and 28.9 ms, for the second cycle are 121 mm and 21.6 ms, for the third cycle are 103 mm and 17.5 ms. (*b*) Close-up of (*a*) for time 0.0–4.0 ms.

where t_{ARR} and t_{MAX} are the time taken for the reflected wave to arrive and the time taken for the bubble to expand to its maximum size, $R(t)$ is the bubble radius measured from high-speed photographic images, W_0 and W_r are the work done by $p_{atm} + p_H - p_v$ and p_r, respectively. When the pressure and radius time history in figure 3(*a*) are used in (4), W_r is 7.1 % of W_0. Because R_{MAX} is approximately one-third the order of magnitude of W_0, the influence on R_{MAX} from reflection waves is given by a 2.4 % difference. In reality, reflected waves do not approach from all directions and W_r in (4) can be treated as the upper bound of the interference of reflection pressure. This value is within the error range of the image, so the interference of reflection waves can be ignored.

3. Results and discussion

The experimental data from all test conditions were processed to draw a figure similar to figure 3(*a*). From these results bubble behaviour, including bubble period, radius variation, migration, and jetting may be analysed and compared with those of cavitation bubbles.

3.1. *Bubble period and radius in free field*

A simple one-dimensional equation can compute the dynamics of a spherical bubble oscillating in a free field:

$$\frac{p_b - p_\infty}{\rho} = \frac{3}{2}(\dot{R})^2 + R\ddot{R}. \tag{5}$$

This is the simplest form of the Rayleigh–Plesset equation where p_b is the pressure inside the bubble, $p_b = p_g + p_v$, p_g is the pressure of the gas inside bubble, p_∞ is the ambient pressure and $p_\infty = p_{atm} + p_H$, ρ is the fluid density. The dot above R indicates that it is a time derivative. Although this is a simplified equation, its solution fits excellently with the FF spark bubble (Chahine, Frederick & Lambrecht 1995). It may be further assumed the gas inside the bubble follows the polytropic law, that is

$$p_{g0} V_0^K = p_g V^K, \tag{6}$$

where p_{g0} and V_0 are the initial gas pressure and volume of bubble, respectively, and K is the polytropic index. Substituting (6) into (5), neglecting p_v because it is relatively small and replacing V_0 with the cube of the initial radius of the bubble R_0^3 gives

$$p_{g0}\left(\frac{R_0}{R}\right)^{3K} - p_\infty = \rho\left[\frac{3}{2}(\dot{R})^2 + R\ddot{R}\right]. \tag{7}$$

Note that p_{g0} and R_0 relate to each other according to the following:

$$p_{g0} = \frac{3(1-K)}{1-\left(\dfrac{R_0}{R_{MAX}}\right)^{3K-3}}\left[\frac{p_\infty}{3}\left(1-\left(\frac{R_0}{R_{MAX}}\right)^{-3}\right)\right]. \tag{8}$$

In (7), R_0 and K are unknown. Chahine *et al.* (1995) introduced a procedure to find R_0 and K by best fitting of R_{MAX} and t_B. Figure 4 shows the images of the bubble collapsing under the FF test condition. From these images it can be seen that the bubble shape is spherical until the last moment before collapse; (7) may be applied to compute its motions. Because solid explosives become gas immediately after ignition, R_0 and R_{MAX} can be found from the dimensions of the detonator and figure 3(*a*). For

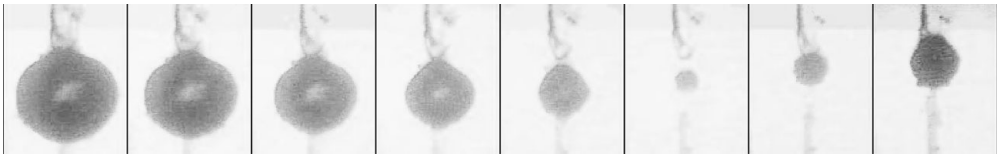

FIGURE 4. High-speed photographs of bubble collapse under the FF condition ($D = 1.5$ m, frame interval = 0.186 ms, image width = 200 mm).

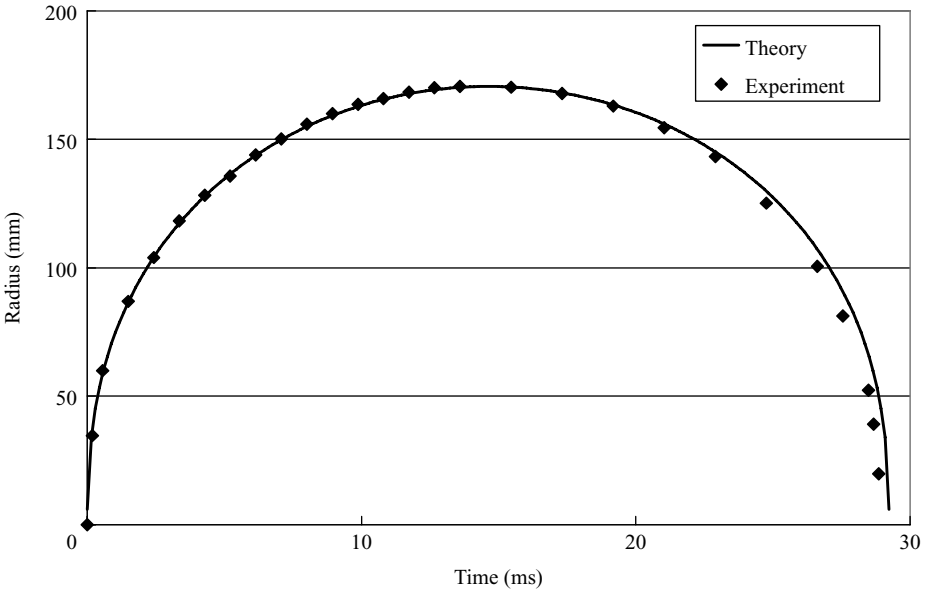

FIGURE 5. The comparison between the solution of (7) with $K = 1.667$ and experimental data.

$R_0 = 5.99$ mm and under the assumption that the initial speed of the radius is zero, K becomes the only unknown.

If the procedure of Chahine *et al.* (1995) is followed, the value of K will exceed the reasonable range of $1.25 \leqslant K \leqslant 1.667$. Therefore, the value $K = 1.667$ is chosen in this work. This results in $p_{g0} = 1.751 \times 10^9$ Pa (254 000 psi), which is of the same order of magnitude as TNT with $K = 1.333$, where p_{g0} is 8.963×10^8 Pa (130 000 psi; Keil 1961). Figure 5 compares the solution of (7) with experimental data. The contraction stage is shown to differ; experimental data give a faster contraction stage than (7) with a period that is approximately 1.2 % shorter. Soh & Karimi (1996) conducted simulations and found that the ideal gas bubble has a higher heat transfer rate than that of a vapour bubble, which may explain the difference in contraction stages. The content of a spark/laser generated bubble is closer to a vapour bubble, while for an UNDEX bubble the content is similar to an ideal gas bubble. In the Rayleigh–Plesset equation an adiabatic condition is assumed; therefore, the bubble with a smaller heat transfer rate may better fit its solution. The heat transferred into water results in a decrease in the internal energy of the bubble. In the contraction stage, this energy loss is acute which may explain why the contraction is faster in practice than in the theory which does not account for heat loss.

Another comparison of energy loss is that which occurs during the bubble collapse and rebound. The ratio of bubble energy in different cycles can be estimated from

the cube of the bubble period (Lee *et al.* 2007):

$$\frac{E_{n+1}}{E_n} = \left(\frac{t_{B,n+1}}{t_{B,n}}\right)^3, \tag{9}$$

where E_n and $t_{B,n}$ are the bubble energy and the period of the nth cycle, respectively. Energy loss in the bubble collapse and rebound are the major parts of bubble energy loss. For an UNDEX bubble in figure 3(*a*), E_2/E_1 is 42 %, and other UNDEX bubbles are also near this value (Cole 1948; Klaseboer *et al.* 2005); for a spark bubble E_2/E_1 is 22 % (Lee *et al.* 2007). The reason for greater energy loss may be that the contents of the bubble are different. For a laser bubble, the contents are all derived from water during the expansion phase; they are argon (Ar), nitrogen (N_2) and oxygen (O_2), which come from dissolved air and H_2O (Didenko & Suslick 2005). When bubbles contract, these contents will burn off to form soluble products, and initial products include hydroxyl radicals $OH^{\cdot}$ and nitrogen oxides (NO_x), and then a series of chemical reactions follow (Yasui *et al.* 2005). Ideally, all the products of these reactions dissolve in the surrounding water before the end of the collapse and recover Ar, N_2, O_2 and H_2O to their initial condition on expansion. But the temperature and pressure are not as high as before because of the energy dissipation, so the amounts of these initial contents are less than those of the last expansion; this will further reduce the bubble energy. The contents of an UNDEX bubble are mainly from the explosive and most of them will not dissolve in the water when the bubble contracts, so the bubble energy lost will relatively be less than a laser bubble. The authors believe that the spark bubble will display similar results to a laser bubble.

From the ratio of R_{MAX}/R_0 another difference between an UNDEX and a laser bubble can be found. In figure 3(*a*), the ratio is approximately 28, while the ratio for a laser bubble is about 5–10 (Ohl, Lindau & Lauterborn 1998). This can be explained because UNDEX bubbles begin with explosive and spark/laser bubbles begin with nothing, so UNDEX not only has a much violent primary shock but also has a greater amount of gas to develop a bigger bubble.

3.2. *Bubble shape and period near the boundary*

When a bubble oscillates near a boundary, the bubble shape and t_B will change. Fundamentally, except for small γ, the bubble remains spherical in the expansion stage. During the contraction, especially just before the collapse, the bubble has various shapes depending on the boundary conditions and γ. Figures 6–11 show these different bubble shapes near different boundaries.

As mentioned earlier, the UNDEX bubble behaves in a similar manner to the spark/laser bubble macroscopically. In figure 6, the bubble is split into two parts by annular flow. A laser bubble near the boundary of PAA (polyacrylamide) with 80 % water content at $\gamma = 0.38$ in Brujan *et al.*'s (2001*b*) experiment has a similar behaviour. The bubble shapes in figures 8 and 9 are the same as those of a laser bubble near a 95 % and 70 % PAA boundary at $\gamma = 0.33$ and 0.41 (Brujan *et al.* 2001*b*).

The bubble period t_B also varies with boundary conditions and stand-off. For the convenience of comparison, t_B is normalized. The non-dimensional bubble period τ^* is defined as

$$\tau^* = \frac{t_B}{t_{OSC}}, \tag{10}$$

where t_{OSC} is the Rayleigh oscillation time of a bubble in a free field and is usually applied as the theoretical bubble period in cavitation study. The definition of t_{OSC} is

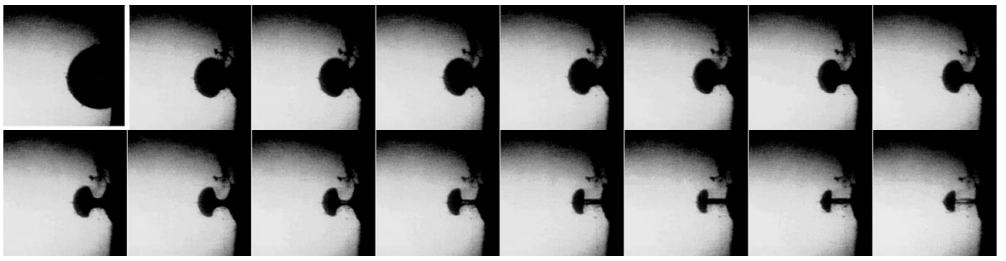

FIGURE 6. Bubble shape before collapse, 10 mm Al plate boundary, $\gamma = 0.54$, $D = 2.55$ m, frame interval = 0.2 ms, image width = 500 mm, first image is the bubble at maximum. The right wall of the bubble sticks to the boundary upon contact. The flow near the boundary is blocked, and the flow pattern thus changes from radial to annular. This annular flow squeezes the right half part of the bubble centripetally as the bubble contracts. The flow near the middle part of the bubble is faster than that near the boundary, which is almost zero; the bubble is cut into two parts by this annular flow. The left part of the bubble becomes a torus before collapse.

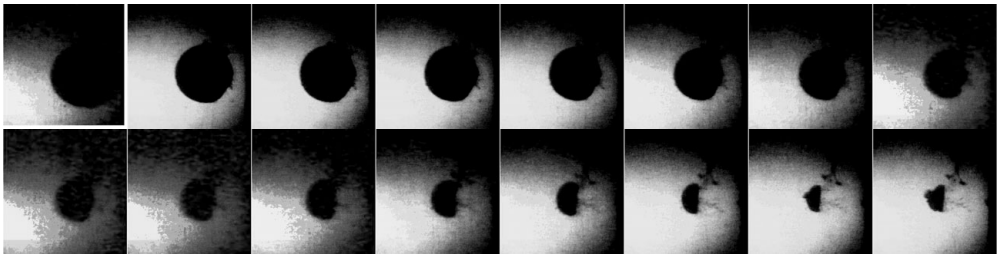

FIGURE 7. Bubble shape before collapse, 10 mm Al plate boundary, $\gamma = 0.96$, $D = 2.55$ m, frame interval = 0.5 ms, image width = 500 mm; first image is the bubble at maximum.

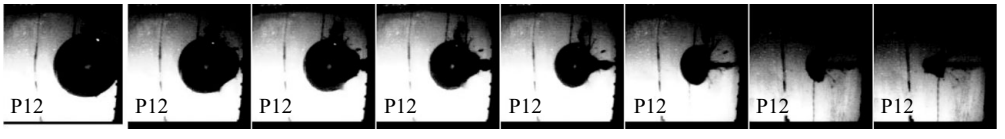

FIGURE 8. Bubble shape before collapse, 5 mm Al plate boundary, $\gamma = 0.63$, $D = 2.55$ m, frame interval = 1 ms, image width = 500 mm; first image is the bubble at maximum. The bubble is in contact with the boundary in the early stage of expansion and then separates. The annular flow causes a circular concave shape on the right hemisphere and drives it to shrink faster than the left bubble. The circular concave shape expands and flattens the right hemisphere; then the bubble profile becomes a semicircle. A protrusion appears at the left bubble and the trace between the right bubble and the boundary in the last frame reveal the jet shooting from right to left almost horizontally.

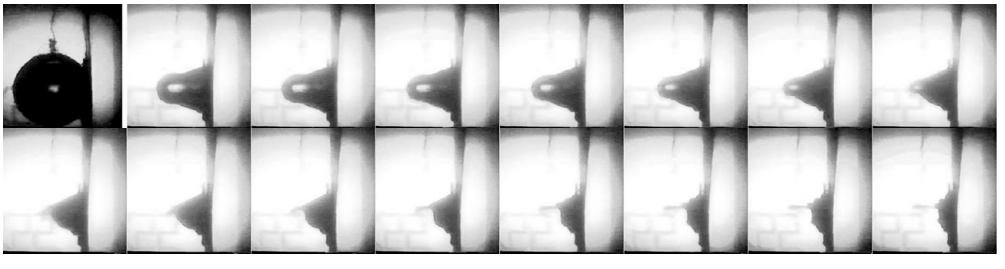

FIGURE 9. Bubble shape before collapse, 2FI boundary, $\gamma = 0.71$, $D = 1.5$ m, frame interval = 0.2 ms, image width = 500 mm; first image is the bubble at maximum.

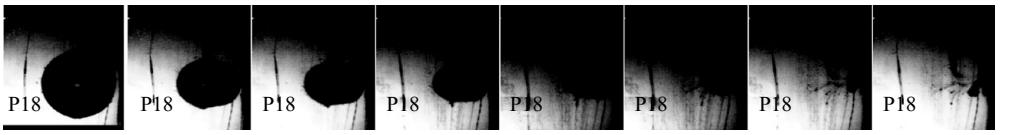

FIGURE 10. Bubble shape before collapse, 35 mm St plate boundary, $\gamma = 0.96$, $D = 2.55$ m, frame interval = 1 ms, image width = 500 mm; first image is the bubble at maximum.

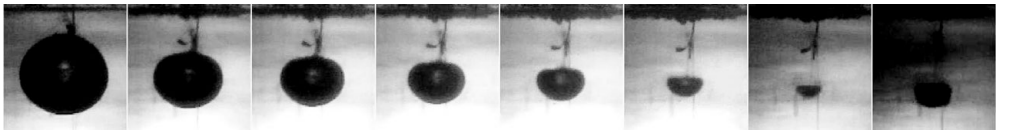

FIGURE 11. Bubble shape before collapse, FS boundary, $\gamma = 1.51$, $D = 0.283$ m, frame interval = 1 ms, image width = 500 mm; first image is the bubble at maximum.

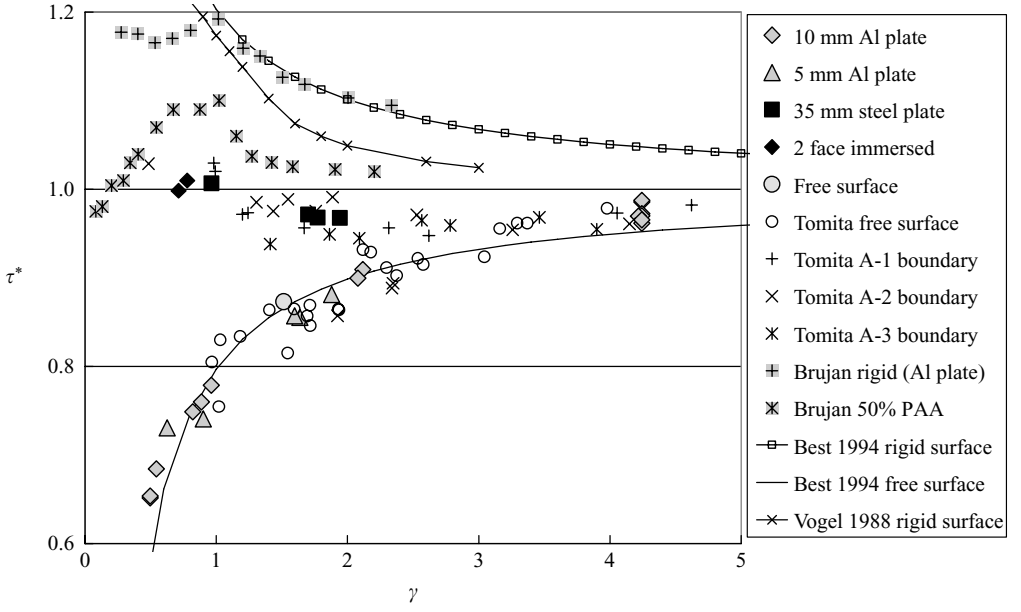

FIGURE 12. Variations of τ^* near different boundaries with respect to γ.

(Rayleigh 1917)

$$t_{OSC} = 1.83 \left(\frac{\rho}{p_\infty - p_v} \right)^{1/2} R_{MAX}. \tag{11}$$

Figure 12 shows the τ^* variations near different boundaries with respect to γ; data from other references are included for comparison. In figure 12 the trends of τ^* under the 10 and 5 mm Al plate conditions can be seen to be close to the free surface image method line (Best & Blake 1994). The difference between the 10 and 5 mm Al plate conditions is small. Data from Tomita & Kodama's (2003) free surface experiment show similar trends. For τ^* under the St and 2FI conditions, the trend is not close to the image method line of a rigid surface (Best & Blake 1994). Data from the A-1, A-2 and A-3 boundaries of Tomita & Kodama's (2003) experiment show a similar

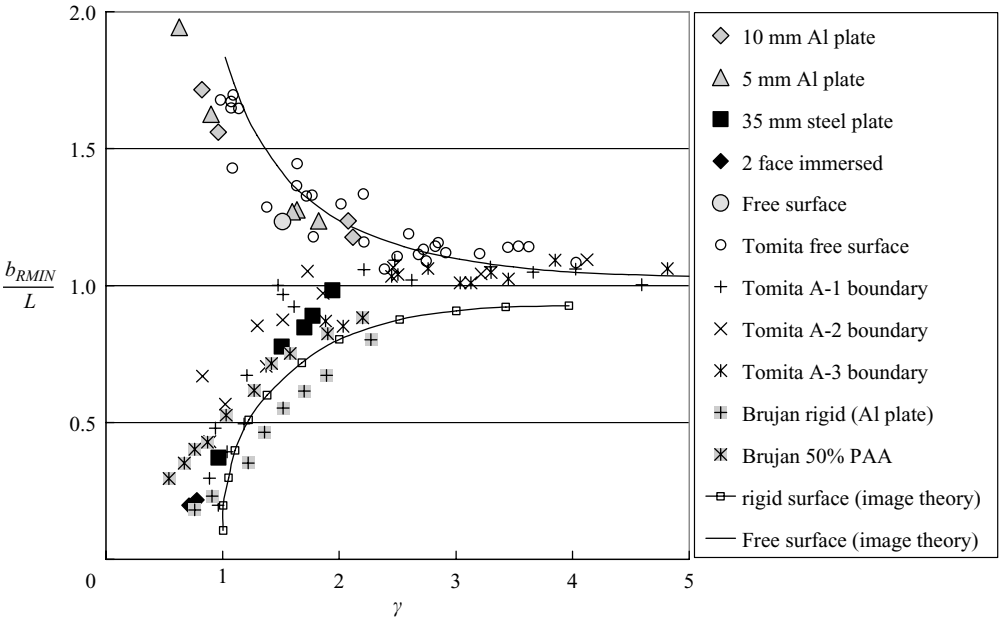

FIGURE 13. Bubble collapse position for various γ values and boundaries.

trend to St and 2FI. Part of Brujan *et al.*'s (2001*b*) rigid surface, which was made by aluminium (Al plate), fit well with Best & Blake's (1994) line. Below this line is the experimental rigid boundary line from Vogel & Lauterborn's (1988) elongation factors.

From figure 12 it is inferred that the Al plate boundaries of this work are in some way relatively flexible to the free surface. On the other hand, St and 2FI boundaries are not comparatively rigid; however, the 50 % PAA and Vogel & Lauterborn (1988) rigid surface are more rigid, while the Al plate used by Brujan *et al.* (2001*b*) is the most rigid boundary relative to all other boundaries shown in this figure.

3.3. *Bubble migration*

Migration is an interesting characteristic of bubbles. Bubble jets and shock waves emitted during collapse can damage boundaries and are related to bubble migration. Therefore, bubbles that migrate towards or away from boundaries have attracted much attention in the research on both UNDEX and cavitation bubbles for a long time. Figure 13 presents the bubble collapse position for various γ values and boundaries. The ordinate is the normalized migration distance b_{RMIN}/L, b_{RMIN} is the distance between the first bubble collapse position and the boundary. Through scaling to L, data from different bubbles can be compared.

The line $b_{RMIN}/L = 1$ represents the border of migration direction. Above this line the bubble migrates away from the boundary and vice versa. Like those in figure 12, the trends of migration under the 10 and 5 mm Al plate conditions are close to the free surface image method line (Kodama & Tomita 2000). The difference between the 10 and 5 mm Al plate conditions is small once again. Data from Tomita & Kodama's (2003) free surface experiment also display the same tendency. Data acquired under the St and 2FI conditions display a trend that is much closer to the rigid surface image method line than in figure 12. Migrations of Brujan *et al.*'s (2001*b*) rigid surface

are over the theory line, and the 50 % PAA data are closer to St and 2FI than to figure 12.

The Kelvin impulse is a useful theoretical framework in predicting migration direction at the end of the bubble collapse. The Kelvin impulse of a bubble is defined as

$$\boldsymbol{I} = \rho \int_{S_b} \Phi \boldsymbol{n} \mathrm{d}s, \tag{12}$$

where S_b is the surface of the bubble, $\boldsymbol{n}$ is the normal vector of S_b and Φ is the velocity potential. The rate of change of the Kelvin impulse is given by (Blake & Cerone 1982; Brujan, Pearson & Blake 2005):

$$\frac{\mathrm{d}\boldsymbol{I}}{\mathrm{d}t} = \boldsymbol{F}^{\Sigma} + \boldsymbol{F}^{g}, \tag{13}$$

with

$$\boldsymbol{F}^{g} = \rho g V \boldsymbol{e}_z, \tag{14}$$

$$\boldsymbol{F}^{\Sigma} = -\rho \int_{\Sigma} \left\{ \frac{1}{2} (\nabla \Phi)^2 \boldsymbol{n} - \frac{\partial \Phi}{\partial n} \nabla \Phi \right\} \mathrm{d}s, \tag{15}$$

where $\boldsymbol{e}_z$ is a unit vector in the z direction (positive upward), $\boldsymbol{F}^g$ is the buoyancy force, $\boldsymbol{F}^{\Sigma}$ is the pressure-gradient Bjerknes force exerted by the boundary and V is the volume of bubble. This is under the assumption that the velocity potential can be expressed by a source with time-varying strength, that is a spherical bubble, and using an image method to simulate the boundary. The Kelvin impulse vector of buoyancy and Bjerknes force at the completion of the collapse phase near the infinite plane boundary are (Blake *et al.* 1986; Blake & Gibson 1987)

$$\boldsymbol{I}^{g} = \frac{4\sqrt{6}\pi R_{MAX}^4 \rho^{3/2} g}{9 (\Delta p)^{1/2}} \beta \left(\frac{11}{6}, \frac{1}{2} \right) \boldsymbol{e}_z, \tag{16}$$

$$\boldsymbol{I}^{\Sigma} = \frac{2\pi R_{MAX}^5 (6 \Delta p \, \rho)^{1/2}}{9 L^2} B \, \beta \left(\frac{7}{6}, \frac{3}{2} \right) \boldsymbol{e}_{\zeta}, \tag{17}$$

where $\Delta p = p_{\infty} - p_v$, $\boldsymbol{e}_{\zeta}$ is a unit normal vector to the boundary with positive directed outward and $\beta(w, z)$ is the beta function. Note that B equals -1 for a rigid boundary, $+1$ for a free surface, and for an inertial boundary $B = H(\alpha), \alpha = \rho L / \sigma$, where σ is the mass per unit area of the boundary, and

$$H(\alpha) = 4\alpha - 1 - 8\alpha^2 \mathrm{e}^{2\alpha} E_1(2\alpha), \tag{18}$$

where E_1 is the exponential integral.

The bubble in this model is stationary. Best & Blake (1994) developed a more sophisticated model to allow the bubble to move towards a rigid surface boundary. For the same conditions, (17) and (18) become

$$\boldsymbol{I}^{g} = \frac{4\sqrt{6}\pi R_{MAX}^4 \rho^{3/2} g}{9(\Delta p)^{1/2}} \left[\beta \left(\frac{11}{6}, \frac{1}{2} \right) + \frac{1}{4\gamma} \beta \left(\frac{13}{6}, \frac{1}{2} \right) \right] \boldsymbol{e}_z, \tag{19}$$

$$\boldsymbol{I}^{\Sigma} = -\frac{2\pi R_{MAX}^5 (6 \Delta p \, \rho)^{1/2}}{9 L^2} \left[\beta \left(\frac{7}{6}, \frac{3}{2} \right) - \frac{1}{4\gamma} \beta \left(\frac{3}{2}, \frac{3}{2} \right) \right] \boldsymbol{e}_{\zeta}. \tag{20}$$

To understand the relationship between the Kelvin impulse and the bubble migration, $\boldsymbol{I}$ is computed from experimental data from this study, together with data from other references. Equations (17)–(21) with $B = H(\alpha)$ is used, which means that elasticity is

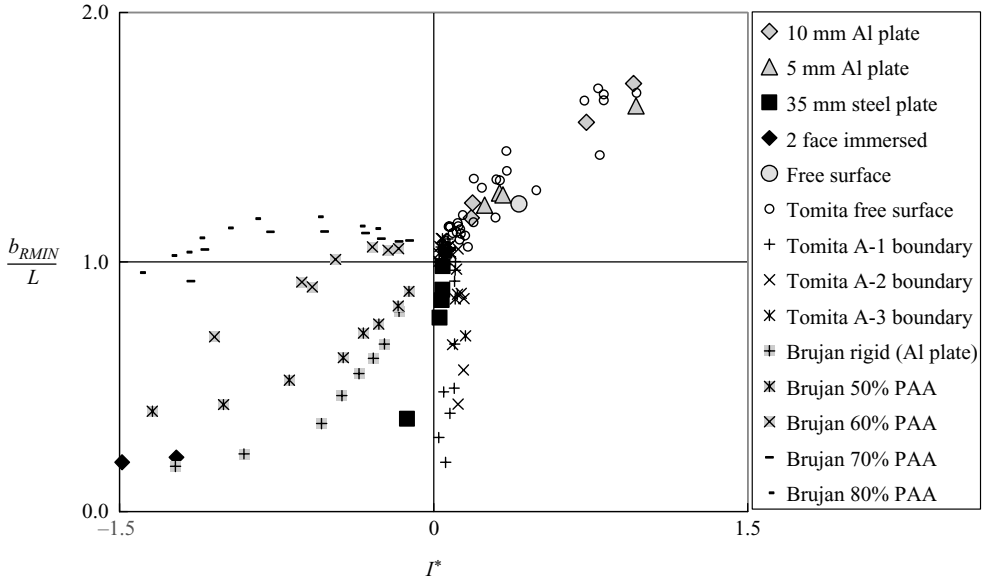

FIGURE 14. The relationship between the Kelvin impulse and the bubble migration.

not considered here. FS conditions use (17) and (18) with $B = 1$, while rigid conditions use (20) and (21). A γ value less than 0.7 will not be used because the computed results are not accurate. For a horizontal boundary $\boldsymbol{e}_z$ and $\boldsymbol{e}_\zeta$ are parallel, $\boldsymbol{I} = \boldsymbol{I}^g + \boldsymbol{I}^\Sigma$, while for a vertical boundary $\boldsymbol{e}_z$ and $\boldsymbol{e}_\zeta$ are perpendicular and only $\boldsymbol{I}^\Sigma$ will be considered. The magnitude of $\boldsymbol{I}$ is scaled according to

$$I_{SC} = \frac{R_{MAX}^3}{(\Delta p\, \rho)^{1/2}}, \tag{21}$$

and is represented by I^*. Figure 14 illustrates the relationship between I^* and b_{RMIN}/L, except the conditions shown in figure 13, and Brujan *et al.*'s (2001*b*) 60 %–80 % PAA data are included. Ideally, data points should be distributed within the first and third quadrant. However, this is not true for all conditions. For cavitation bubbles, I^* predicts well for free surface and rigid boundary conditions, but for the boundary of 70 %, 80 % PAA and Tomita & Kodama's (2003) A-1, A-2 and A-3, I^* fails to be a good predictor. This is not surprising because the simple model of Kelvin impulses, (17)–(21), does not consider elasticity. On the other hand, for the UNDEX bubbles of this work, I^* predicts well in Al conditions. However, Al plates have higher stiffness than the boundaries mentioned above; obviously, the elasticity that causes I^* to fail should be considered as a relative value with respect to bubble size.

Boundary inertia m^* and boundary stiffness k^* are two non-dimensional boundary factors (Gibson & Blake 1982). Shima *et al.* (1989) used these two factors as the abscissa and b_{RMIN}/R_{MAX0} as the ordinate to show their effects on bubble migration. The definition of m^* is

$$m^* = \frac{m_e}{\rho R_{MAX}^3}, \tag{22}$$

where m_e is a partial mass of the boundary corresponding to the maximum bubble project area. We have $m_e = \pi R_{MAX}^2 \rho_b t_b$, where ρ_b and t_b are the density and thickness of the boundary, respectively. Figure 15 illustrates the relationship between m^* and b_{RMIN}/L. From the data of Shima *et al.* (1989) and this work, a tendency for

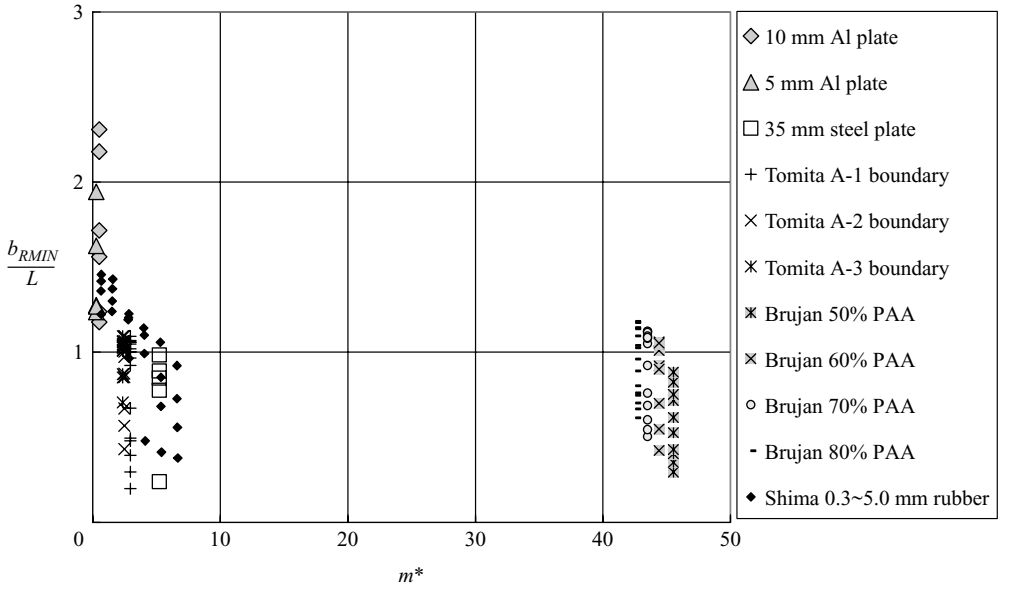

FIGURE 15. The relationship between m^* and the bubble migration.

the direction of bubble migration can be found in the range $0 < m^* < 10$. Shima *et al.* (1989) suggested that it is influenced by γ. But in the range $40 < m^* < 50$, Brujan *et al.*'s (2001*b*) data show a different trend. Although data in the range $10 < m^* < 40$ are missing, the authors infer that the trend of influence of γ should be monotonical; this inconsistency can be treated as more evidence of the influence of elasticity.

The definition of boundary stiffness k^* is

$$k^* = \frac{k}{R_{MAX}^2 \sqrt{\rho \, \Delta p}}, \tag{23}$$

where k is the equivalent spring constant of the boundary. The value of k is determined experimentally by pressing a spherical weight with a certain radius close to R_{MAX} into the boundary and measuring the slope of the load–displacement curve (Shima *et al.* 1989).

Brujan *et al.* (2001*b*) do not provide k in their paper, and it is difficult to apply a spherical load on the steel plate of this work. However, because the boundaries have a simple geometric shape and are of uniform material, a simple finite element model can simulate the system. With the assumption that the boundary material is isotropically elastic, only Young's modulus E and the Poisson ratio υ are needed to model the material. For the Al and St plates, these two values can be found in textbooks. For Brujan *et al.*'s (2001*a*, *b*) PAA, E can be found in their papers, while υ is set to 0.5 (Zhang, Daunert & Foegeding 2005). From the simulation the k values of the Al and St plates were found to be linear in the range of the deflection in the experiment. On the other hand, the PAA load–displacement curve is nonlinear. Because the E of PAA was measured at 10 % strain, the value of k adopted is that at which the maximum strain in PAA is approximately this value. Figure 16 illustrates the relationship between k^* and b_{RMIN}/L. Again in this figure, data from this study and Shima *et al.* (1989) show a similar tendency while the trend of Brujan

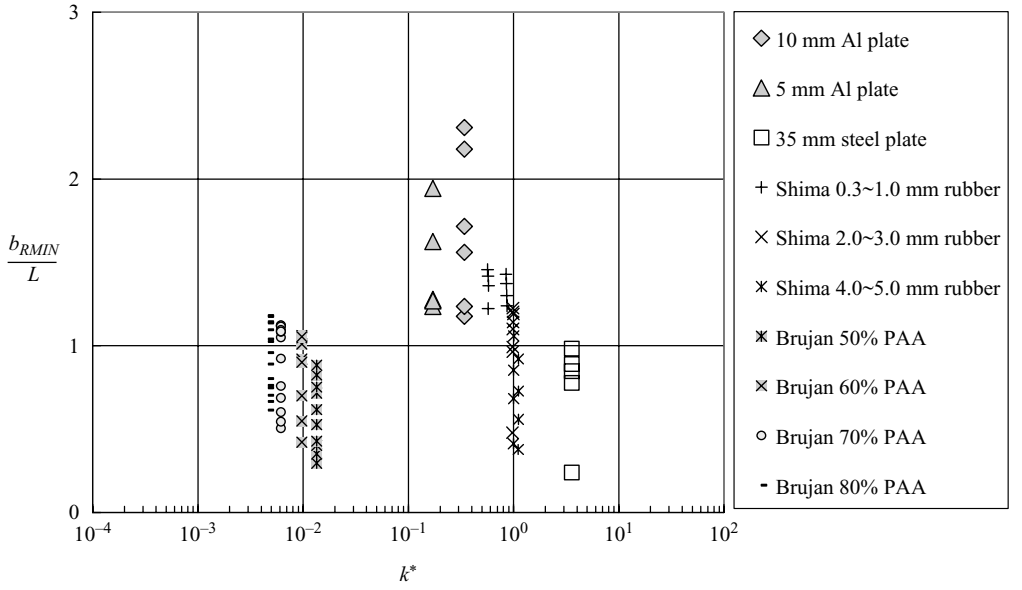

FIGURE 16. The relationship between k^* and the bubble migration.

et al.'s (2001*b*) data are inconsistent with the former. It is inferred that the reason I^* and m^* cannot predict bubble migration comprehensively is that the elasticity is not considered. However, from figure 16 it is known that elasticity is not the only concern in the prediction of migration direction. The migration of the bubble is influenced by boundary inertia, elasticity and stand-off; no one factor can predict migration alone.

The response of the boundary may provide some information about bubble migration. Figure 17 shows the time history of the strain at the boundary centre and the bubble margin distance. The strain gauges were installed on the dry side of the plate. When the boundary plate is concave, the dry side is under tension and the strain is positive; when the boundary plate is convex, strain is negative. The margin distance is the distance between the bubble's left and right margins to the detonation point. Because the boundary is at the right, the right margin distance is positive and the left margin distance is negative. From figure 17, a concave boundary can be seen from the excitation of a primary shock, and the bubble expands at approximately the same time. When the boundary rebounds to convex, the bubble starts to contract and migrates outward. In a way, the bubble is pushed out by the boundary, that is, its motions are in phase. The test condition in figure 17 is 10 mm Al plate, $\gamma = 0.96$, and similar profiles have been observed for other Al plate conditions. The response frequency of the plate is a function of boundary inertia, elasticity and stand-off. From this, the authors infer that the in-phase motion of the boundary and bubble is a predicting index of repulse migration.

A similar situation can be found in Duncan *et al.* (1996), where Shima *et al.*'s (1989) experiment was simulated. From the history of the displacement of the centre node of the boundary surface it can be found that the boundary rebounds when the bubble contracts, and migrates away from the convex boundary.

Under the St plate condition, in-phase motion does not appear because the plate's vibration frequency does not match that of the bubble. Figure 18 is the strain history of the 35 mm St plate and the bubble margin at $\gamma = 0.96$. Under this test condition,

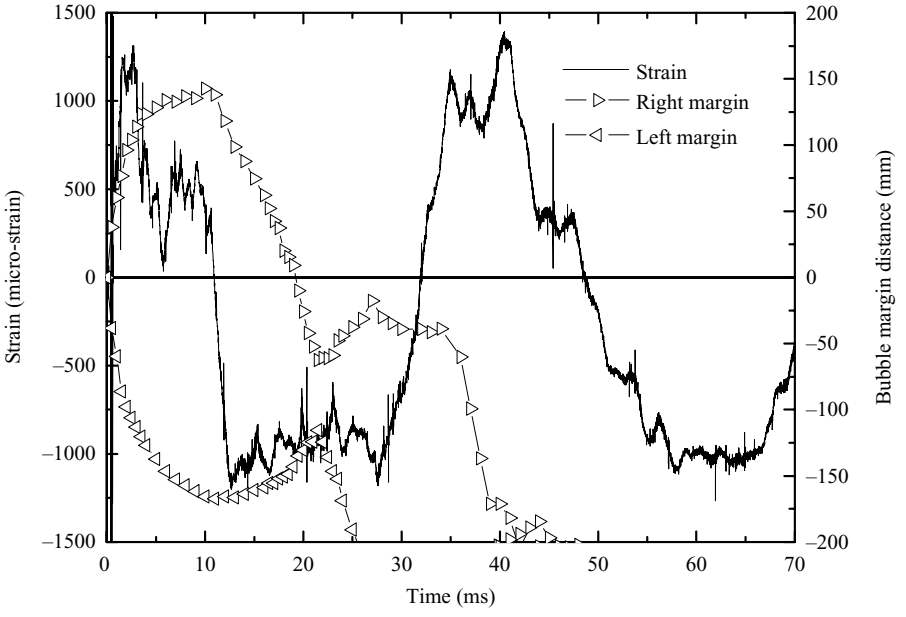

FIGURE 17. The comparison of the history of boundary strain and bubble motion (10 mm Al plate boundary, $\gamma = 0.96$).

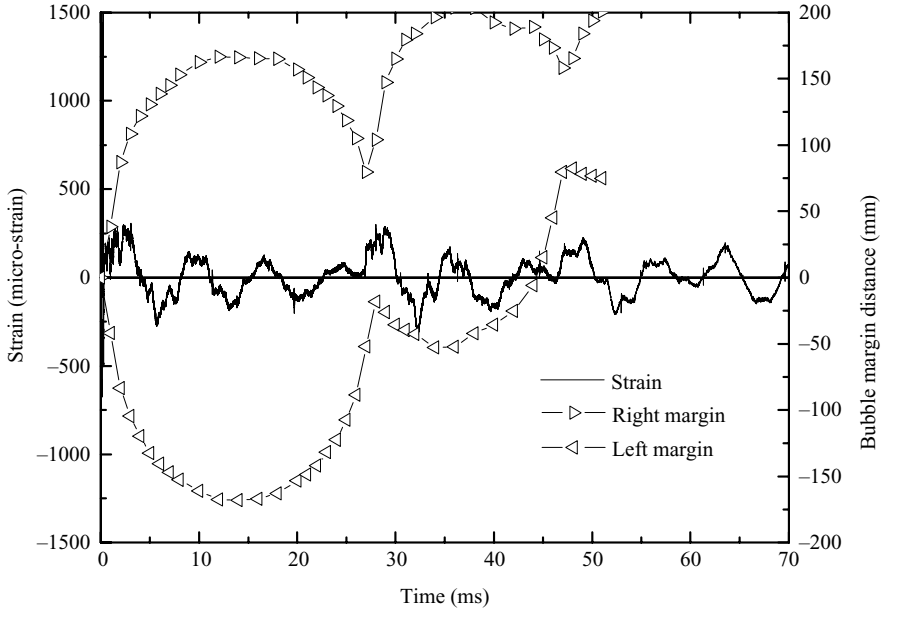

FIGURE 18. The comparison of the history of boundary strain and bubble motion (35 mm St plate boundary, $\gamma = 0.96$).

two bubble collapses are recorded. The vibration frequency of the St plate is about four times higher than that of the bubble. An interesting observation can be made: the magnitude of the vibrating strain decreases consecutively after the primary shock.

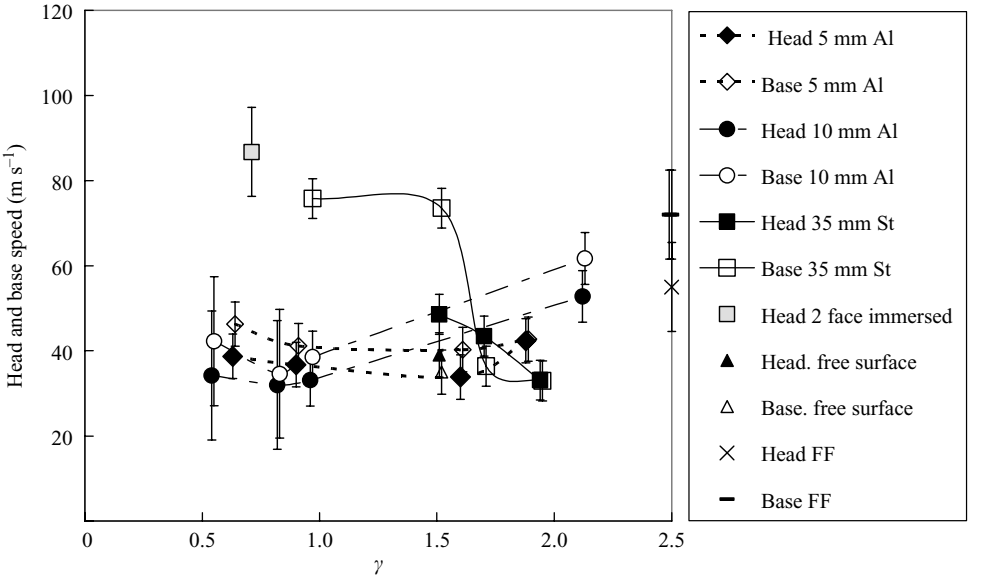

FIGURE 19. Protrusion head speed and concave base speed of torus bubble for various boundaries and stand-offs.

However, at the fifth peak the magnitude increases to about the same level as the first peak, and a larger peak can also be found at the second collapse. The authors believe this is because of the influence of the bubble's collapse. This can provide information on the damageability of the bubble pulse and jet to the nearby structure.

3.4. *Bubble jet*

In the final stage of contraction, a bubble jet is formed on one side of the bubble and penetrates through the opposite side. A concave base and a protrusion can be observed from the bubble's profile. The speeds of the protrusion head and the concave base were measured from the image of the bubble profiles. The errors are estimated according to the accuracy of image analysis (table 2) and it is assumed that there is no error in the time frame. The range of error is between 5 and 15 m s^{-1}. Although the jet tip moves faster and is thinner than the head of the bubble protrusion (Lauterborn & Bolle 1975), the speeds still yield at least the lower bound on, and general variation of, the speed of the jet tip. Figure 19 plots these speeds as functions of γ with error bars. The γ in the case of FF should be infinite; $\gamma = 2.5$ in figure 19.

The data in figure 19 are about one order of magnitude lower than those obtained by Brujan *et al.* (2000*b*). The jet tip speeds in other studies range from 50 to 180 m s^{-1} (Plesset & Chapman 1971; Lauterborn & Bolle 1975; Tomita & Shima 1986; Blake & Gibson 1987), and are of the same order of magnitude as the present results. The speed differences between Brujan *et al.* (2001*a*, *b*) and this work may be due to the temporal resolution of high-speed photography. To capture the high-speed motion, the frame rate is crucial. From these results the authors inferred that the jet tip speed of the UNDEX bubbles and the cavitation bubbles is of the same order.

Except for the FS case, the concave base moves faster than the protrusion head, possibly because the jet loses energy during water penetration. When a jet has

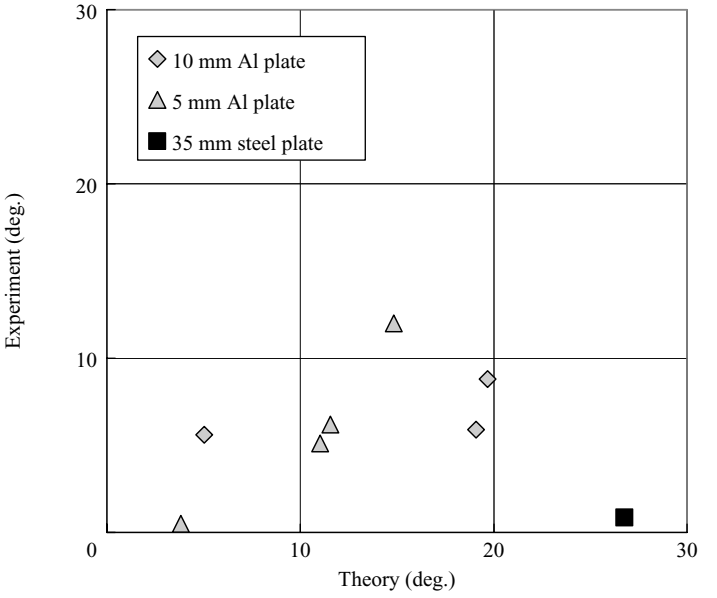

FIGURE 20. The comparison of theoretical and experimental angles of the bubble jet.

just formed at the base of the bubble, it penetrates low-density material inside the bubble.

The Kelvin impulse has two vector components: buoyancy force and Bjerknes force. When the boundary is vertical, the direction of the jet is tangent to these two forces (Best, Soh & Yu 1996). The simple model of the Kelvin impulse cannot predict an elastic boundary accurately. But for those conditions in the first and third quadrant of figure 14, it is interesting to compare the jet angle predicted by theory with that from the experiment. Figure 20 illustrates this comparison; the abscissa is the absolute value of the angle of the tangent of $\boldsymbol{I}^g + \boldsymbol{I}^\Sigma$, the ordinate is the absolute value of the angle of the jet measured from the image; only data where $\gamma > 0.7$ are plotted. Ideally, the data points should lie on the diagonal. However, theoretical jet angles are greater than experimental values, and the greater the stiffness, the greater the discrepancy. This proves the role of elasticity in bubble migration, and it can be seen that the intensity of the influence is directly proportional to stiffness.

3.5. *Further results*

In the preceding sections, the key behaviours of the bubble were discussed. In this section, two minor but interesting points will be examined. The first is the profile of the bubble pulse and the second is an observation of an unlikely boundary jet.

3.5.1. *Profile of bubble pulse*

On some occasions, multiple peaks on the top of bubble pulse curve can be observed, which occurs mostly under an FF condition, conditions with a boundary are not obvious; only one case is found. Figure 21 illustrates this multiple peaks profile under FF (thin line) and 5 mm Al plate $\gamma = 1.89$ (thick line) conditions. Note

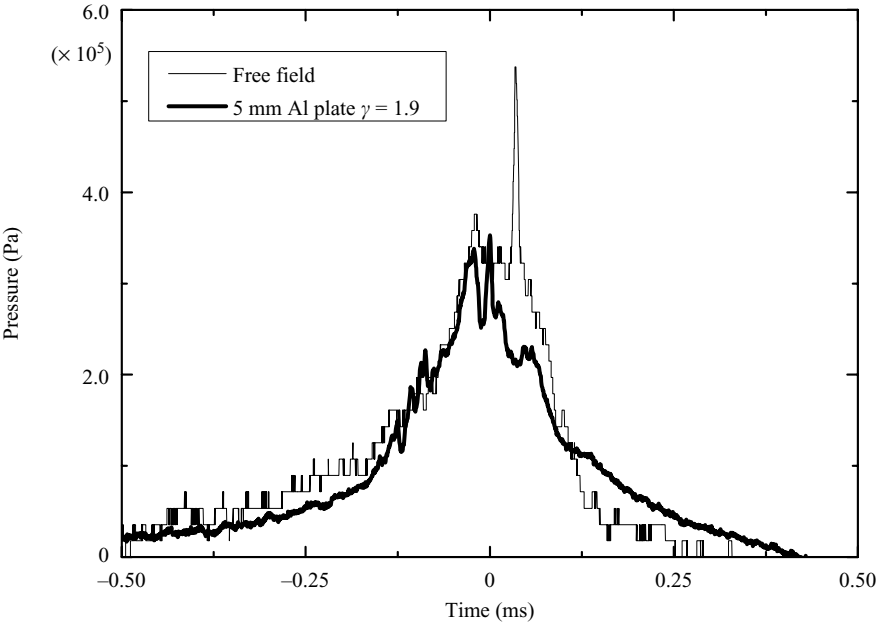

FIGURE 21. The comparison of pressure profile of bubble pulses.

that t_0 is adjusted, so both profiles can be plotted in the same time frame. The profile of FF condition has an especially high peak; this is not a reflection shock as we have seen in figure 3(*b*) because the noise has decayed before the bubble pulse; it is impossible to have such a big reflection peak suddenly.

The profile is different from both Klaseboer *et al.*'s (2005) UNDEX bubble data under an FF condition and horizontal resilient plate conditions, as well as Tomita & Shima's (1986) rigid boundary spark bubble data. However, Tong *et al.*'s (1999) rigid boundary-laser bubble displayed profiles with multiple peaks. A peak in the profile is an indication of impact, it jet impact on the bubble wall or bubble wall impact on itself. The detailed mechanism and sequence of a peak are beyond the scope of this paper. From figure 21 it is noted that multiple impacts may occur in the collapse of an UNDEX bubble as well as laser bubbles.

3.5.2. *Boundary jet*

For $\gamma = 0.63$ and 0.90 under the 5 mm Al plate condition, when a bubble was about to contract to its minimum size, something is observed from the images of high-speed photography to 'shoot out' (figure 22). This resembles the PAA jet from the boundary material of Brujan *et al.*'s (2001*a*) study. However, the Al plate was intact after the experiment; therefore, obviously this is not a boundary jet. Because an annular flow was developed between the bubble and the boundary, the authors infer that when the bubble contracts to its minimum size, the strong annular flow makes the density around its symmetry axis different and refracts the light passing through to create moving shadows which appear to be boundary jets; we hope a simulation is developed in future to explore this phenomenon.

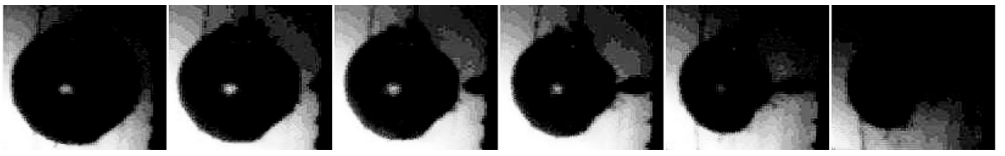

FIGURE 22. Doubtful boundary jet, 5 mm Al plate boundary, $\gamma = 0.90$, $D = 2.55$ m, frame interval = 1 ms, image width = 350 mm.

4. Conclusions

The behaviour of an UNDEX bubble near different boundaries has been studied experimentally. The bubble was generated by a detonator, and its equivalent weight to TNT is about 1.12 g. This charge weight is very small compared to other studies of UNDEX bubbles. High-speed photography, underwater pressure gauge and strain gauges were used to measure the bubble behaviour. To understand the differences between UNDEX and spark/laser bubbles, a detailed analysis has been conducted. From the results, the following conclusions can be made.

The UNDEX bubble has a faster contraction speed than spark/laser bubbles under free field conditions (figure 5). Perhaps this is because the contents of UNDEX bubbles are reaction products that are hotter and the heat exchange rate is higher than that in a spark/laser bubble. The contents of spark/laser bubbles are all derived from water and the reaction products of these contents are dissolvable, so the spark/laser bubbles have a much greater energy loss during collapse than the UNDEX bubble. The period difference is about 1.2 % and can be ignored in general applications, such as the use of radius and period equations. But when considering the energy loss during collapse, the spark/laser bubble loses about 20 % more than an UNDEX bubble.

For bubbles near the boundary, the UNDEX and spark/laser bubbles display similar behaviours, including the bubble splitting, annular flow, bubble shape when near a boundary and bubble jetting. The jet tip speeds of both are in the same order.

The tendencies of τ^* versus γ (figure 12) and b_{RMIN}/L versus γ (figure 13) for UNDEX and spark/laser bubbles near different boundaries are also similar. The spacing of data between the Al plate conditions and the free surface condition of spark/laser bubble is very close in both figures. However, the spacing of data between the St plate and 2FI conditions and other boundaries of spark/laser bubble is significantly different in figure 12, that is, the influence of differing boundaries can be distinguished. However, in figure 13, the data points are quite close. The reason for this is not clear; perhaps is because of the elasticity of the boundary.

The simple model of the Kelvin impulse I^* can predict migration well when a bubble is near a free surface or a rigid boundary. But as I^* does not consider elasticity, it fails to be a good predictor when the boundary has elasticity. This elasticity is a relative value with respect to the bubble size. Boundary inertia m^* and boundary stiffness k^* are also not good indicators. Because I^* considers inertia and stand-off, m^* only considers inertia and k^* only considers stiffness, the migration function must involve all of these parameters. From the response of the strain of the boundary surface, the authors find that the phase between the local vibration and bubble motion could be an index for the prediction of migration. When both are in phase, the bubble is pushed away by, or migrates away from, the boundary. The phase motion is connected to the natural frequency of the boundary, which is a function of the inertia and elasticity and could provide an explanation of bubble migration. The authors wish to explore this further in later studies

B boundary characteristic function in the Kelvin impulse equation
b_{RMIN} distance from first bubble collapsed position to the boundary
D detonation depth
E Young's modulus
E_n bubble energy of the n-th cycle
$\boldsymbol{e}_z$ unit vector in z direction
$\boldsymbol{e}_\zeta$ unit vector normal to the boundary
$\boldsymbol{F}^g$ buoyancy force of the Kelvin impulse
$\boldsymbol{F}^\Sigma$ Bjerknes force of the Kelvin impulse
$H(\alpha)$ inertial boundary characteristic function in the Kelvin impulse equation, $\alpha = \rho L/\sigma$
$\boldsymbol{I}$ the Kelvin impulse
I_{SC} scale factor of the vector coefficient of the Kelvin impulse
I^* non-dimensional vector coefficient of the Kelvin impulse
K polytropic index
k^* boundary stiffness
L stand-off, distance between boundary and detonation point
m_e partial mass of the boundary corresponding to the maximum bubble project area
m^* boundary inertia
$\boldsymbol{n}$ normal vector of S_b
p_{atm} atmospheric pressure
p_b pressure inside bubble
p_g pressure of the gas inside bubble
p_{g0} initial pressure of the gas inside bubble
p_H hydraulic pressure
p_r reflected wave
p_v vapour pressure in water
p_∞ ambient pressure, $p_\infty = p_{atm} + p_H$
$R(t)$ bubble radius
R_{MAX} maximum bubble radius
R_{MAX0} the average of maximum bubble radius
R_0 initial radius of bubble
S_b surface of bubble
t_B bubble period
$t_{B,n}$ bubble period of the n-th cycle
t_b thickness of boundary
t_{MAX} the time bubble expand to its maximum size
T_{ARR} the time the reflected wave arrive
t_{OSC} Rayleigh oscillation time for bubble in free field $t_{OSC} = 1.83(\frac{\rho_l}{p_\infty - p_v})^{1/2} R_{MAX}$
V volume of bubble
V_0 initial volume of bubble
W_0 work done of $p_{atm} + p_H - p_v$
W_r work done of p_r
Φ velocity potential
γ non-dimensional stand-off $\gamma = L/R_{MAX0}$
ρ fluid density
ρ_b density of boundary
σ mass per unit area of boundary
τ^* non-dimensional bubble collapse time $\tau^* = t_B/t_{OSC}$
υ Poisson ratio

REFERENCES

Best, J. P. 1993 The formation of toroidal bubbles upon the collapse of transient cavities. *J. Fluid Mech.* **251**, 79–107.

Best, J. P. & Blake, J. R. 1994 An estimate of the Kelvin impulse of a transient cavity. *J. Fluid Mech.* **261**, 75–93.

Best, J. P., Soh, W. K. & Yu, C. F. 1996 An experimental investigation of buoyant transient cavity collapse near rigid cylindrical boundaries. *J. Fluids Engng* **118**, 195–198.

Blake, J. R. & Cerone, P. 1982 A note on the impulse due to a vapour bubble near a boundary. *J. Austral. Math. Soc.* B **23**, 383–393.

Blake, J. R. & Gibson, D. C. 1987 Cavitation bubbles near boundaries. *Annu. Rev. Fluid Mech.* **19**, 99–123.

Blake, J. R., Taib, B. B. & Doherty, G 1986 Transient cavities near boundaries. Part 1. Rigid boundary. *J. Fluid Mech.* **170**, 479–497.

Blake, J. R., Taib, B. B. & Doherty, G 1987 Transient cavities near boundaries. Part 2. Free surface. *J. Fluid Mech.* **181**, 197–212.

Brujan, E. A., Nahen, K., Schmidt, P. & Vogel, A. 2001*a* Dynamic of laser-induced cavitation bubbles near a elastic boundary. *J. Fluid Mech.* **433**, 251–281.

Brujan, E. A., Nahen, K., Schmidt, P. & Vogel, A. 2001*b* Dynamics of laser-induced cavitation bubbles near a elastic boundary: influence of the elastic modulus. *J. Fluid Mech.* **433**, 283–314

Brujan, E. A., Pearson, A. & Blake, J. R. 2005 Pulsating, buoyant bubbles close to a rigid boundary and near the null final Kelvin impulse state. *Intl J. Multiphase Flow* **31**, 302–317

Chahine, G. L., Frederick, G. S. & Lambrecht, C. J. 1995 Spark-generated bubbles as laboratory-scale models of underwater explosions and their use for validation of simulation tools. In *SAVIAC 66th Proc. Shock and Vibration Symp.*, Biloxi, MS, vol. 2, pp. 265–276.

Chisum, J. E. & Shin, Y. S. 1997 Explosion gas bubbles near simple boundaries. *Shock Vib.* **4** (1), 11–25.

Cole, R. H. 1948 *Underwater Explosions*. Princeton University Press.

Didenko, Y. T. & Suslick. 2005 The energy efficiency of formation of photons, radicals and ions during single-bubble cavitation. *Nature* **418**, 394.

Duncan, J. H., Milligan, C. D. & Zhang, S. 1996 On the interaction between a bubble and a submerged compliant structure. *J. Sound Vib.* **197** (1), 17–44.

Gibson, D. C. & Blake, J. R. 1982 The growth and collapse of bubbles near deformable surfaces. *Appl. Sci. Res.* **38**, 215–224.

Goertner, J. F., Hendrickson, J. R. & Leamon, R. G. 1969 Model studies of the behaviour of underwater explosion bubbles in contact with a rigid bottom. *NOL Tech. Rep.* NOLTR-68-207, AD851749.

Hammond, L. & Grzebieta, R. 2000 Structural response of submerged air-backed plate by experimental and numerical analyses. *Shock Vib.* **7**, 333–341.

Hooton, M. C., Blake, J. R. & Soh, W. K. 1993 Behaviour of an underwater explosion bubble near a rigid boundary: theory and experiment. *In Bubble Dynamics and Interface Phenomena. Proc. IUTAM Symp., Birmingham, U.K.*, pp. 421–428.

Hung, C. F. & Hsu, P. Y. 2003 Non-linear dynamic response of submerged plate subjected to underwater explosion. *J. SNAME-ROC* **22** (4), 201–212.

Hung, C. F., Hsu, P. Y. & Hwangfu, J. J. 2005 Elastic shock response of an air-backed plate subjected to underwater explosion in water tanker. *J. Impact Engng* **31**, 151–168.

Hwangfu, J. J. 2004 Experimental study of the influence of UNDEX shock factor to the strain and acceleration of structure. In *Proc. Society of Explosives and Propellants ROC Symp., Taipei, Taiwan*, pp. 199–211 (in Chinese).

Keenan, J. H., Keyes, F. G., Hill, P. G. & Moore, J. G. 1969 *Steam Table*. John Wiley.

Keil, A. H. 1961 Response of ship to underwater explosions. *SNAME Trans.* **69**, 366–410.

Klaseboer, E., Hung, K. C., Wang, C., Wang, C. W., Khoo, B. C., Boyce, P., Debono, S. & Charlier, H. 2005 Experimental and numerical investigation of the dynamics of an underwater explosion bubble near a resilient/rigid structure. *J. Fluid Mech.* **537**, 387–413.

Kodama, T. & Tomita, Y. 2000 Cavitation bubble behavior and bubble shock wave interaction near a gelatin surface as a study of in vivo bubble dynamics. *Appl. Phys.* B **70**, 139–149.

Lauterborn, W. & Bolle, H. 1975 Experimental investigations of cavitation–bubble collapse in the neighbourhood of a solid boundary. *J. Fluid Mech.* **72** (2), 391–399.

Lee, M., Klaseboer, E. & Khoo, B. C. 2007 On the boundary integral method for the rebounding bubble. *J. Fluid Mech.* **570**, 407–429.

Lindau, O. & Lauterborn, W. 2003 Cinematographic observation of the collapse and rebound of laser-produced cavitation bubble near wall. *J. Fluid Mech.* **479**, 327–348.

Menon, S. 1996 Experimental and numerical studies of underwater explosions. *Annu. Rep.* N00014-91-J-1993.

Naude, C. F. & Ellis, A. T. 1961 On the mechanism of cavitation damage by nonhemispherical cavities collapsing in contact with a solid boundary. *Trans. ASME* D*: J. Basic Engng* **83**, 648–656.

Ohl, C. D., Lindau, O. & Lauterborn, W. 1998 Luminescence from spherically and aspherically collapsing laser induced bubbles. *Phys. Rev. Lett.* **80** (2), 393–396.

Plesset, M. S. & Chapman, R. B. 1971 Collapse of an initially spherical vapour cavity in the neighbourhood of a solid boundary. *J. Fluid Mech.* **47**, 283–290.

Rajendran, R. & Narasimhan, K. 2001 Linear elastic shock response of plane plate subject to underwater explosion. *Intl J. Impact Engng* **25**, 493–506.

Ramajeyathilagam, K. & Vendhan, C. P. 2004 Deformation and rupture of thin rectangular plates subjected to underwater shock. *Intl J. Impact Engng* **30**, 699–719

Ramajeyathilagam, K, Vendhan, C. P. & Rao, V. B. 2000 Non-linear transient dynamic response of rectangular plates under shock loading. *Intl J. Impact Engng* **24**, 999–1015.

Rayleigh, L. 1917 On the pressure developed in a liquid during the collapse of a spherical cavity. *Phil. Mag.* **34**, 94–98.

Rentz, T. R. 1984 Experimental investigation onto the dynamic response of a stiffened flat plat loaded impulsively by an underwater shockwave. NPS master thesis.

Shima, A., Tomita, Y., Gibson, D. C. & Blake, J. R. 1989 The growth and collapse of cavitation bubbles near composite surfaces. *J. Fluid Mech.* **203**, 199–214.

Soh, W. K. & Karimi, A. A. 1996 On the calculation of heat transfer in a pulsating bubble. *Appl. Math. Model.* **20**, 639–645.

Tomita, Y. & Kodama, T. 2003 Interaction of laser-induced cavitation bubbles with composite surfaces. *J. Appl. Phys.* **94** (5), 2809–2816.

Tomita, Y. & Shima, A. 1986 Mechanisms of impulsive pressure generation and damage pit formation by bubble collapse. *J. Fluid Mech.* **160**, 535–564.

Tong, R. P., Schiffers, W. P., Shaw, S. J., Blake, J. R. & Emmony, D. C. 1999 The role of 'splashing' in the collapse of a laser-generated cavity near a rigid boundary. *J. Fluid Mech.* **380**, 339–361.

Vogel, A. & Lauterborn, W. 1988 Acoustic transient generation by laser-produced cavitation bubbles near solid boundaries. *J. Acoust. Soc. Am.* **84** (3), 719–730.

Wilkerson, S. 1993 Boundary integral technique for explosion bubble collapse analysis. ARL-TR-184, AD-A267369.

Yasui, K., Tuziuti, T., Sivakumar, M. & Iida, Y. 2005 Theoretical study of single-bubble sonochemistry. *J. Chem. Phys.* **122**, 224706.

Zhang, J., Daunert, C. R. & Foegeding, F. A. 2005 Characterization of polyacrylamide gels as an elastic model for food gels. *Rheol. Acta.* **44**, 622–630.